The Astrophysical Journal, 823:45 (15pp), 2016 May 20 doi:10.3847/0004-637X/823/1/45

TIME-DEPENDENT SUPPRESSION OF OSCILLATORY POWER IN EVOLVING SOLAR MAGNETIC FIELDS

S. Krishna Prasad [1], D. B. Jess[1,2], R. Jain[3], and P. H. Keys [1,4]
[1] Astrophysics Research Centre, School of Mathematics and Physics, Queen's University Belfast, Belfast, BT7 1NN, UK; krishna.prasad@qub.ac.uk
[2] Department of Physics and Astronomy, California State University Northridge, Northridge, CA 91330, USA
[3] School of Mathematics and Statistics, University of Sheffield, Sheffield S3 7RH, UK
[4] Solar Physics and Space Plasma Research Centre (SP^{2}RC), The University of Sheffield, Hicks Building, Hounsfield Road, Sheffield S3 7RH, UK
Received 2016 February 5; accepted 2016 March 20; published 2016 May 20

ABSTRACT

Oscillation amplitudes are generally smaller within magnetically active regions like sunspots and plage when compared to their surroundings. Such magnetic features, when viewed in spatially resolved power maps, appear as regions of suppressed power due to reductions in the oscillation amplitudes. Employing high spatial- and temporal-resolution observations from the Dunn Solar Telescope (DST) in New Mexico, we study the power suppression in a region of evolving magnetic fields adjacent to a pore. By utilizing wavelet analysis, we study for the first time how the oscillatory properties in this region change as the magnetic field evolves with time. Image sequences taken in the blue continuum, G-band, Ca II K, and Hα filters were used in this study. It is observed that the suppression found in the chromosphere occupies a relatively larger area, confirming previous findings. Also, the suppression is extended to structures directly connected to the magnetic region, and is found to get enhanced as the magnetic field strength increased with time. The dependence of the suppression on the magnetic field strength is greater at longer periods and higher formation heights. Furthermore, the dominant periodicity in the chromosphere was found to be anti-correlated with increases in the magnetic field strength.

Key words: Sun: chromosphere – Sun: evolution – Sun: magnetic fields – Sun: oscillations – Sun: photosphere

Supporting material: animation

1. INTRODUCTION

The surface amplitudes of *p*-mode acoustic oscillations have been known to be significantly smaller within magnetically active regions compared to those in the surrounding quiet Sun (Leighton et al. 1962; Woods & Cram 1981; Lites et al. 1982; Tarbell et al. 1988; Title et al. 1992). Consequently, magnetic regions are highlighted by locations of reduced power in frequency-filtered power maps. Several theories have been proposed to explain such power suppression. By studying the power difference of waves traveling inward and outward of sunspots, Braun et al. (1987) found that sunspots absorb as much as 50% of the incident acoustic waves. It was suggested that the absorbed power could either be scattered or lost due to the mode coupling of magnetoacoustic or pure magnetic waves. More recently, it has been proposed that the absorption mechanism involves partial conversion of *p*-modes into slow magnetoacoustic waves, which are channeled by magnetic fields and lost into the solar interior (Cally 1995; Cally et al. 2003; Crouch & Cally 2003). Also, convection is largely inhibited in locations of strong magnetic field (Chandrasekhar 1952), as evidenced in recent sunspot simulations (Schüssler & Vögler 2006; Rempel et al. 2009), hence the excitation of *p*-modes by turbulent convection (Goldreich & Keeley 1977; Goldreich & Kumar 1988) is less likely to be efficient in highly magnetic regions. Alternatively, it has been suggested that the acoustic wave functions are modified in the presence of magnetic fields in such a way that the attenuation length of the evanescent *p*-modes is reduced in the solar atmosphere (Jain et al. 1996; Hindman et al. 1997). This mechanism reduces the observed oscillation amplitudes in magnetic regions without any loss of the actual *p*-mode power. A related effect has been discussed in Bogdan & Judge (2006), where the authors demonstrate that the existence of wave sources at greater depths in the umbral regions results in reduced oscillatory power at the surface. The possible differences in the line formation heights associated with magnetic and non-magnetic environments that will naturally give rise to different observed amplitudes have also been discussed previously (Hindman & Brown 1998; Jain & Haber 2002).

As observations progress to higher cadences it has been observed that at high frequencies (>5 mHz) the power is in fact enhanced surrounding magnetic regions (Braun et al. 1992; Brown et al. 1992; Jain & Haber 2002; Moretti et al. 2007; Rajaguru et al. 2013). Similar behavior was observed around quiet-Sun network magnetic elements (Krijger et al. 2001; Kontogiannis et al. 2010; Chitta et al. 2012). At larger heights in the atmosphere, enhanced suppression is found at higher frequencies surrounding the active region (Muglach 2003) and quiet-Sun (Judge et al. 2001; Vecchio et al. 2007; Kontogiannis et al. 2010; Gupta et al. 2013) magnetic fields. Although the exact physical mechanism responsible for these phenomena is not yet clear, currently, the most popular theory that explains the observed features at both low and high frequencies is the interaction of acoustic *p*-mode oscillations with the embedded magnetic fields, which generates fast and slow magnetoacoustic waves in the magnetic canopy through the process of mode conversion (Moretti et al. 2007; Kontogiannis et al. 2014; Rijs et al. 2016).

For this work, our main focus is on the suppression of oscillatory power within the magnetic regions at low frequencies. It has been demonstrated by Hindman & Brown (1998) and Jain & Haber (2002) that low-frequency power suppression increases with magnetic field strength for both Doppler velocity and continuum intensity data. Using multi-height observations, Moretti et al. (2007) observed that the spatial extent of the suppression region increases with height in the solar atmosphere. More recently, through theoretical

modeling work, Jain et al. (2014) predicted that the power deficit in the suppression region also increases with height. Here, we investigate these aspects using our high spatial- and temporal-resolution observations in four different channels, which were obtained simultaneously with the Dunn Solar Telescope (DST). We performed a time-dependent study of the oscillatory power suppression related to a small evolving magnetic concentration that is part of an active region. We present the details of our observations and data preparation in Section 2, the applied analysis methods and results in Section 3, and finally discuss the important conclusions of this work in Section 4.

2. OBSERVATIONS

High-resolution images of active region NOAA 11372 were obtained with the Rapid Oscillations in the Solar Atmosphere (ROSA; Jess et al. 2010) and the Hydrogen-Alpha Rapid Dynamics camera (HARDcam; Jess et al. 2012a) instruments at the DST in New Mexico on 2011 December 10 for about two hours starting from 17:51 UT. Simultaneous observations were made in four different channels: blue continuum (52 Å bandpass centered at 4170 Å), G-band (9.2 Å bandpass centered at 4305.5 Å), Ca II K line core (1 Å bandpass centered at 3933.7 Å), and Hα line core (0.25 Å bandpass centered at 6562.8 Å), using HARDcam for Hα and three identical ROSA cameras for the other lines. The ROSA continuum and G-band filters correspond to a minimum formation height of 25 and 100 km (Jess et al. 2012b), respectively, whereas the Ca II K line core forms below 1300 km (Beebe & Johnson 1969) and the Hα line core originates near 1500 km (Vernazza et al. 1981) above the photosphere. Note that these heights are only representative, as the exact determination of line formation height is quite complex, particularly in the chromosphere (for e.g., see the review by Rutten 2007).

All the images were subjected to speckle reconstruction, among other post-processing routines, as detailed in Keys et al. (2014). The final processed cadences were 2.11 s for the continuum and G-band data, 14.81 s for the Ca II K data, and 1.78 s for the Hα data. For each data set, the counts in each image were normalized to the median of that image to remove any variations in brightness due to changes in the inclination of the Sun during the observations. The seeing conditions remained excellent throughout the duration of observations, except for a brief spell of short-term atmospheric fluctuations that affected a small number of images, which were manually identified and replaced through interpolation. A series of calibration images, taken along with the science observations, were used to coalign the data across the different channels. This step brings all the data to a common plate scale (i.e., that of the blue continuum), which involved interpolating the Hα data to match.

The corresponding line of sight (LOS) magnetograms, obtained from the Helioseismic and Magnetic Imager (HMI; Schou et al. 2012) onboard the *Solar Dynamics Observatory* (*SDO*; Pesnell et al. 2012), are also used in this study. HMI data were processed following the standard `hmi_prep` routine available through *SolarSoft*. The final pixel scale and cadence of the data were approximately 0.″6 and 45 s, respectively. The required coalignment between the HMI and ROSA data was achieved by cross-correlating the ROSA blue continuum and HMI continuum images. This process determined the exact plate scale of the ROSA images to be 0.″0592 per pixel. Samples of the images for each channel are shown in Figure 1. The overplotted contours represent the HMI LOS magnetic fields corresponding to 500 and 950 G, and highlight the accuracy of the coalignment between the various channels and instruments.

3. ANALYSIS AND RESULTS

Figure 1 shows sample images relating to a portion of active region NOAA 11372 as seen in the ROSA and HARDcam channels. The displayed field of view encompasses two pores of the same polarity, one close to the center and the other at the top-left corner. We consider a subfield region outlined by the dashed box in these images, which covers the central pore. These data are then subjected to wavelet analysis (Torrence & Compo 1998) at each pixel in order to study the spatial distribution of oscillatory power across different period bands. Results of the wavelet analysis are shown in Figure 2. Different rows in this figure correspond to different imaging channels. The first and second columns display actual intensities at the start of the time sequence and those averaged over time, respectively. Power maps in three different period bands (2–4, 4–6, and 6–10 minutes) are displayed in the last three columns, which show the corresponding time-averaged oscillatory power present in these bands. The overplotted contours outline the LOS magnetic field at 500 and 950 G, at the start of the sequence (for the first column), and averaged over time (for the rest of the columns).

All the power maps clearly show suppression of oscillatory power across all bands at the location of the pore. Interestingly, there is another patch of suppression of similar size visible in the top-left quarter in Ca II K and Hα power maps. This appears to be connected to a fairly small magnetic concentration in this region, as evident from the magnetic field contours. It must be noted that this small magnetic element would easily have been overlooked in visual inspections of the actual magnetograms had it not been for the associated power suppression. In fact, it has been shown that the suppression of surficial acoustic power can be used to probe subsurface magnetic fields well before their emergence (Hartlep et al. 2011). Thus, to study in detail the observed power suppression and its relation to the underlying small magnetic elements, we consider an additional subfield outlined by the dashed box in Figure 2. Inspection of a timelapse movie of HMI LOS magnetic fields reveals that the smaller magnetic patch in this subfield is constantly evolving from a thin and linear structure at the start of the observations, through to a near circular concentration at the end. One must note that the spatial resolution of HMI is approximately 10 times more coarse compared with ROSA, which can potentially mask other even smaller magnetic concentrations, if present.

The evolution of the average magnetic field in this region is shown in Figure 3. The black line in the bottom panel represents the average taken over the entire subfield, while the red line represents the average taken only from strongly magnetic pixels (i.e., from locations where the magnetic field strength $>$950 G). It appears that the strong field average increases with time, even in the later stage when the average for the whole region has decreased. This suggests more of a reorganization of magnetic flux, rather than the actual emergence of a new magnetism. The top panel in this figure shows the time–distance map generated from the location of the vertical green line marked in Figure 2. Contours outlining locations with magnetic field strengths $\geqslant$500 G and $\geqslant$950 G are

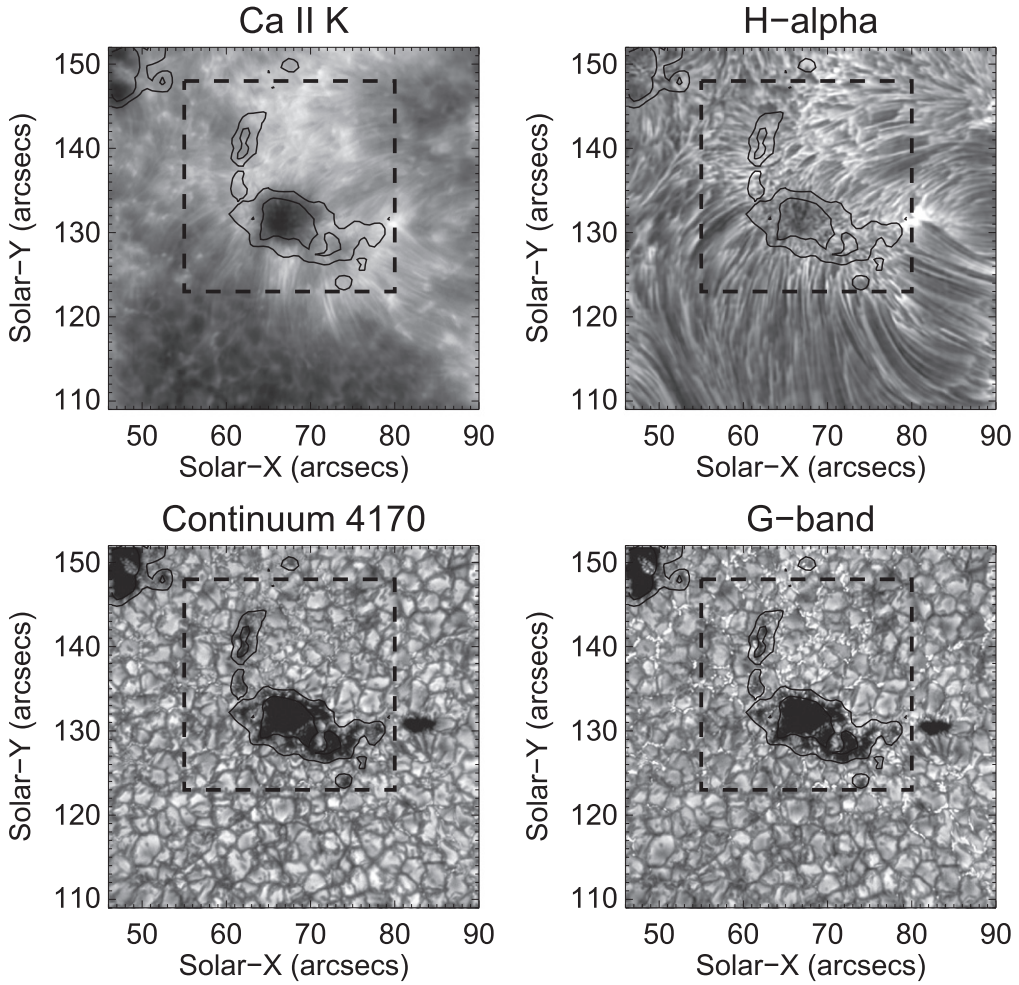

Figure 1. Sample images of a portion of the active region NOAA 11372, as observed with the ROSA and HARDcam instruments across four different channels. The overplotted contours, outer and inner, enclose the locations of HMI LOS magnetic fields, with strengths $\geqslant$500 G and $\geqslant$950 G, respectively. The dashed box highlights the subfield region chosen for creating the power maps shown in Figure 2.

also overplotted on this map. It is evident that the vertical extent of the magnetic element is gradually collapsed until the end of the time sequence, where it forms a more concentrated patch. A time lapse movie of the magnetic field in this region is provided online to clearly show this behavior.

3.1. Time-resolved Power maps

To understand how the evolving magnetic field in the subfield (outlined by dashed box) in Figure 2 influences the oscillatory power in this region, we extract the time-dependent power from wavelet analysis to construct power maps at different instants for the same 2–4, 4–6, and 6–10 minute period bands. Figures 4–7 display these time-dependent power maps at five different instants in time for the blue continuum, G-band, Ca II K, and Hα channels, respectively. In each of these figures, power maps for discreet bands are shown in the bottom three rows, with the corresponding intensity image displayed in the top row. Respective magnetic field contours for 500 and 950 G are also shown using white contours. Each column in these figures represents a time-resolved snapshot of the observations, as specified at the top of each column. The continuum and G-band results (Figures 4 and 5) show more suppression in the vicinity of the magnetic field as its magnitude becomes stronger and more organized. As already highlighted, one must also consider the difference in the spatial resolutions between the various instruments before trying to make a one-to-one correspondence between the power suppression regions in the ROSA power maps and the HMI magnetic fields.

The Ca II K and Hα results (Figures 6 and 7) also show clear evidence for suppression in all period bands at all instants. However, the suppression region appears to be larger and asymmetrically distributed toward the left of the magnetic patch. This appears to be a consequence of the horizontal magnetic canopy structures extending toward the left side, as evident in the Hα intensity images. The remarkable structuring visible in the suppression regions of the Hα power maps is also worth noting. The spatial extent of the power suppression increases with height above the photosphere in agreement with the findings of Moretti et al. (2007). However, this is the first time it has been observed in higher regions of chromosphere using Ca II K and Hα images.

3.2. Time–Distance Power maps

The time-resolved power maps shown in the previous subsection for five different instants of time revealed the spatial distribution and extent of power at different times spanning the magnetic field evolution. However, to get a clearer picture of

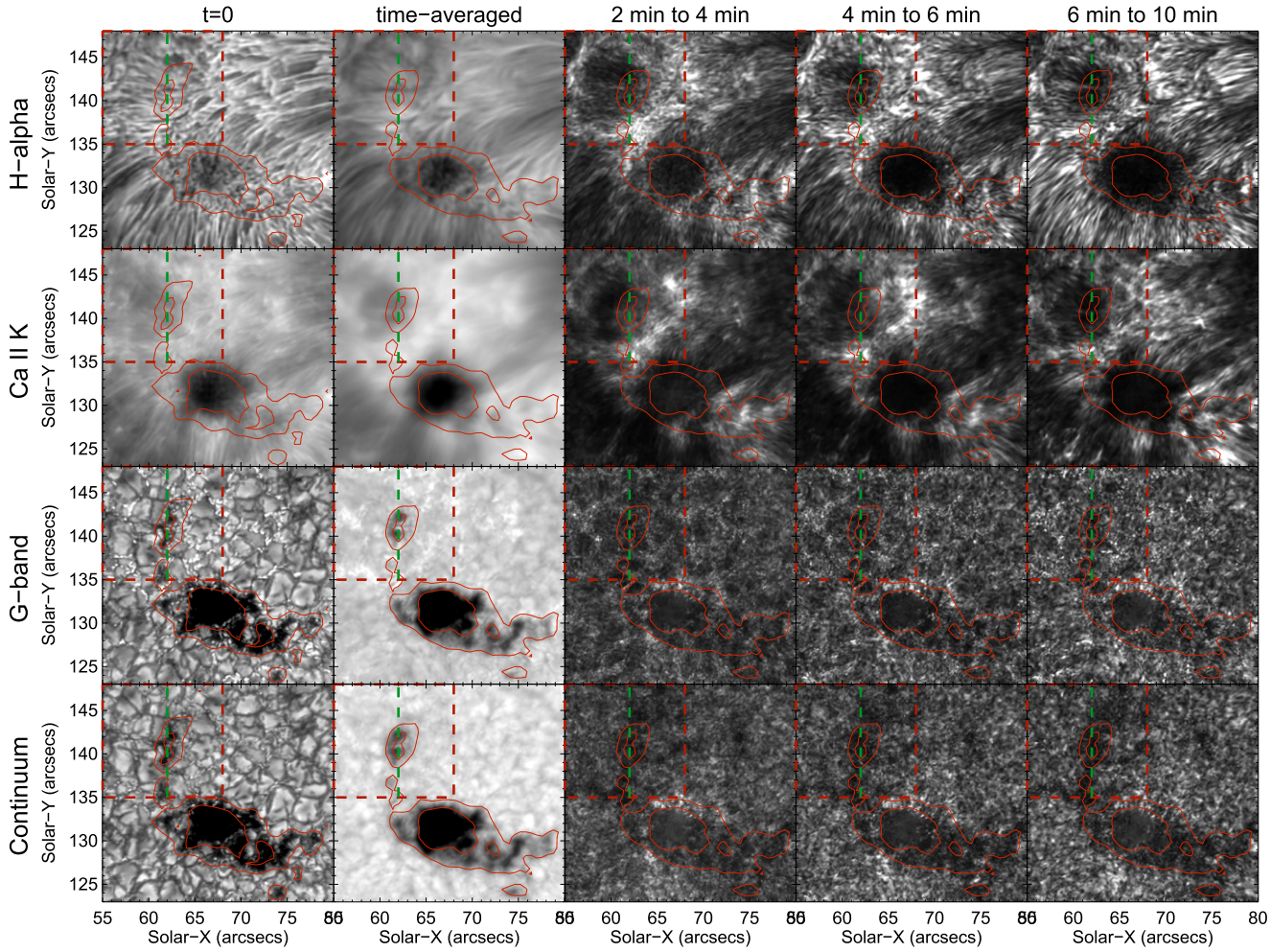

Figure 2. The columns (from left to right) show the intensities at the start time, time-averaged intensities, and power maps in three different period bands: 2–4, 4–6, and 6–10 minutes, for four different imaging channels as labeled. The overplotted contours represent the HMI LOS magnetic field as described in Figure 1. The dashed red box and the vertical green line mark the locations of subsequent analysis. Darker and brighter regions in the power maps highlight locations of lower and higher oscillatory power, respectively.

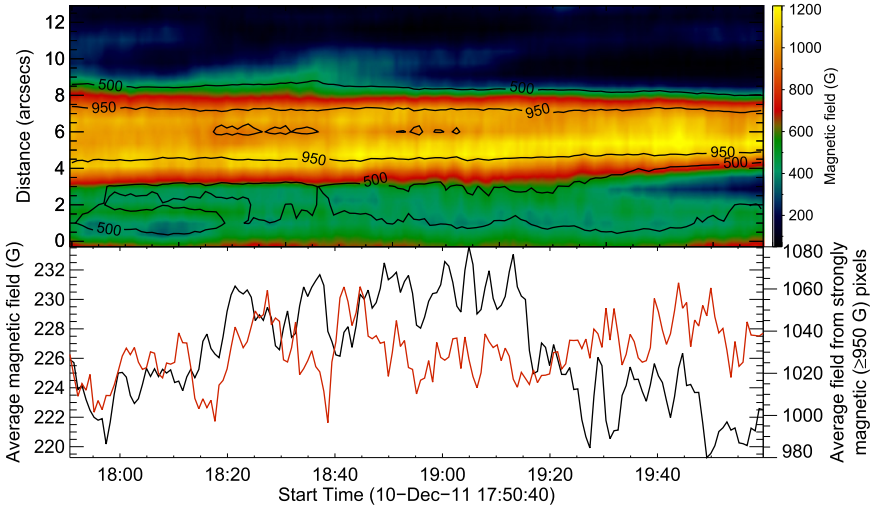

Figure 3. Evolution of the magnetic field within the subfield region outlined by a dashed box in Figure 2. Bottom: the black line represents the average magnetic field over the full subfield, while the red line shows the average computed only from strongly magnetic pixels (≥950 G; inner contours). The axis for the red line is shown on the right. Top: time–distance representation of the magnetic field extracted from the locations marked by the vertical green line in Figure 2. Distance "0" corresponds to the bottom of the slit, while the applied color scaling is shown on the right. Also, the temporal location of the 500 and 950 G field strengths is highlighted through overplotted contours. The animation shows the spatial distribution of the magnetic field and its evolution.

(An animation of this figure is available.)

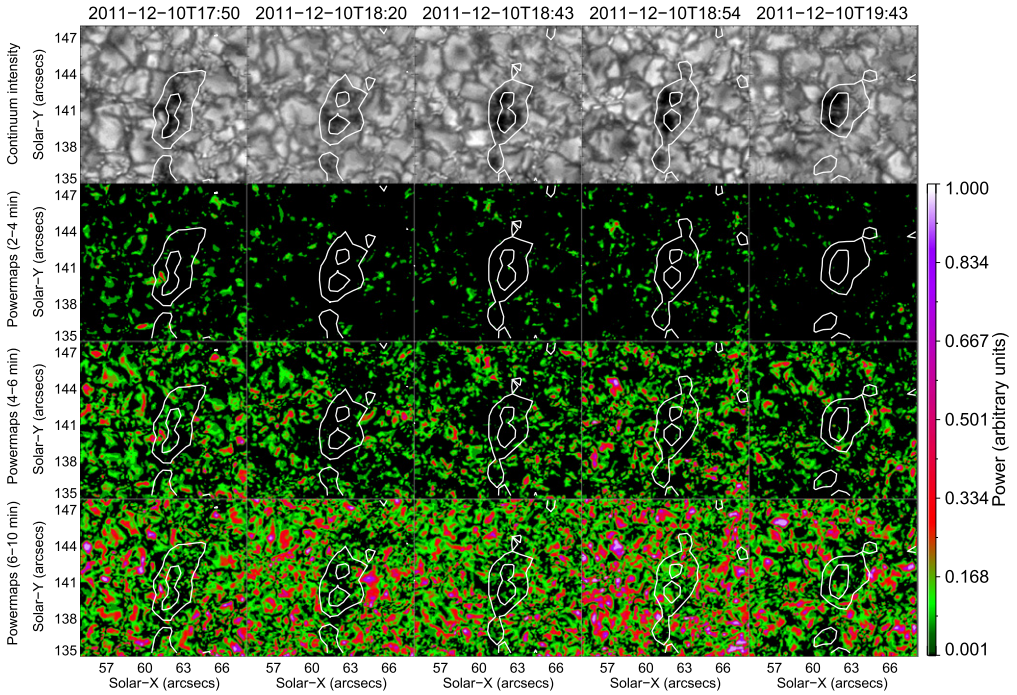

Figure 4. Time-resolved power maps and the respective intensity images from the continuum channel at five different instants during the observations. Each column displays results for a particular instant in time (shown at the top), while rows from the bottom to top display power maps in 6–10, 4–6, and 2–4 minutes, with the top row revealing the corresponding intensity. The contours overplotted denote the locations of magnetic fields at 500 and 950 G, as obtained from the nearest-time HMI LOS magnetogram. Oscillation power can be seen to be suppressed in the magnetic region. A single color scale (shown on right) is used for all the period bands, which highlights the decrease in power with time, in addition to revealing lower oscillatory power at shorter periods.

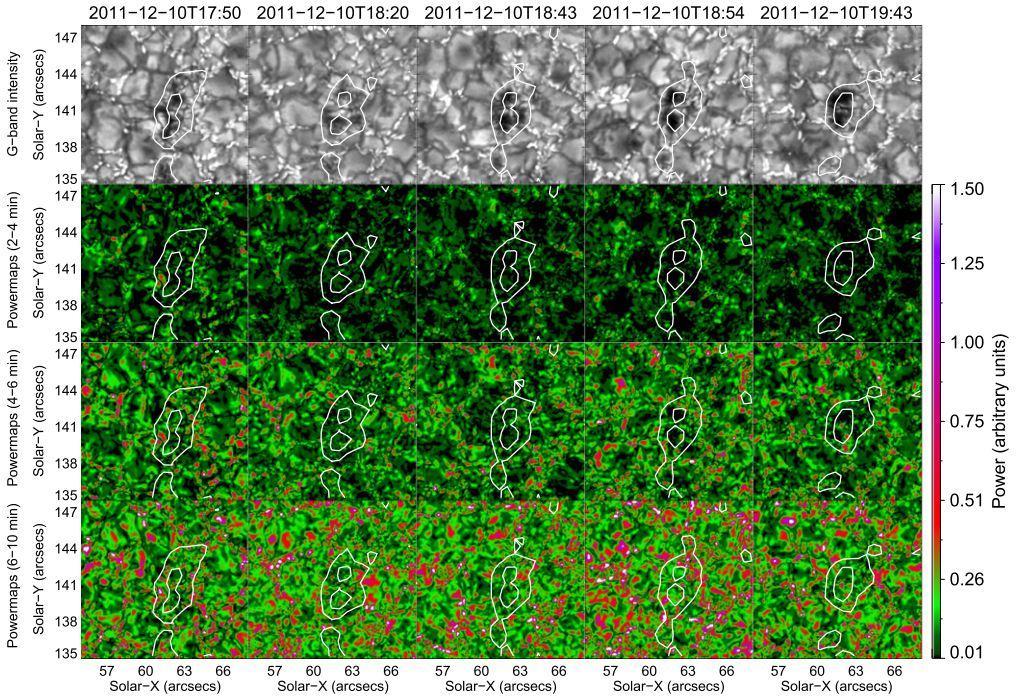

Figure 5. Time-resolved power maps and the respective intensity images for the G-band channel. Descriptions of the individual panels are the same as those described in Figure 4. Intensity images highlight G-band bright points at the intergranular lanes. Power suppression properties are similar to those observed in the continuum channel.

the time-dependent nature of the power suppression with the evolving field, we constructed time–distance power maps. To produce these, we considered a 10 pixel wide slit (≈0.″592 or 430 km) placed on top of the time-resolved power maps, as shown by the dashed green line marked in Figure 2, and averaged the power lying across the slit. The obtained time–distance power maps, along with the corresponding intensity plots, are shown in Figures 8–11 for the continuum, G-band, Ca II K, and Hα channels, respectively. The overplotted contours on these figures enclose the corresponding spatial

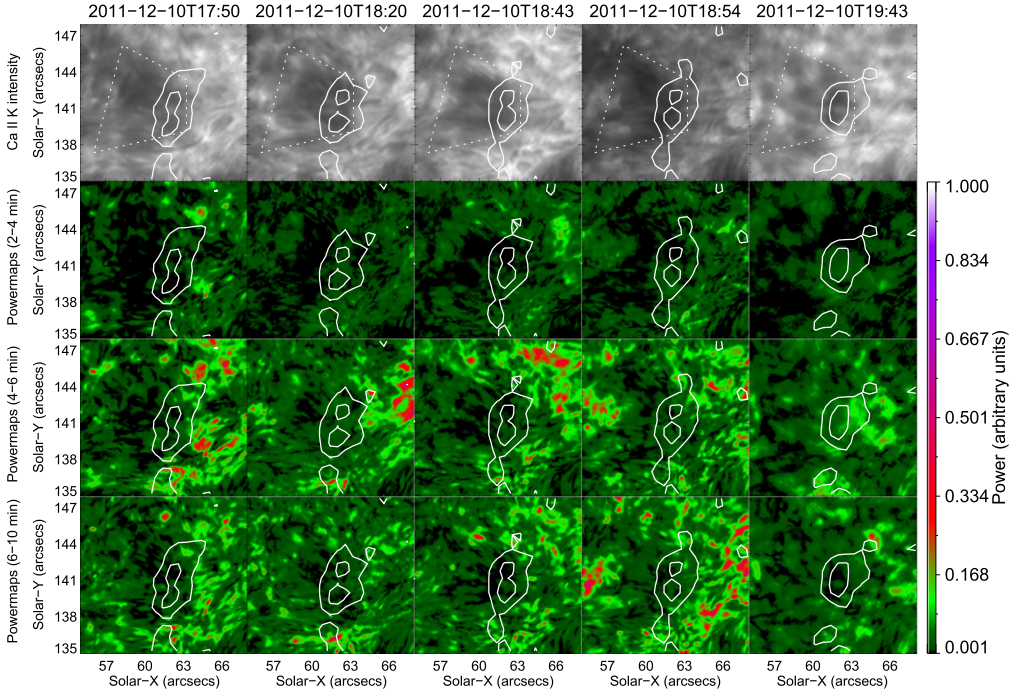

Figure 6. Time-resolved power maps and the respective intensity images for the Ca II K channel. Descriptions of the individual panels are the same as those described in Figure 4. The power suppression appears to be spatially extended and asymmetrically distributed toward the left side of the magnetic region. The polygon marked over the intensity images roughly encloses the power suppression region used in subsequent analysis.

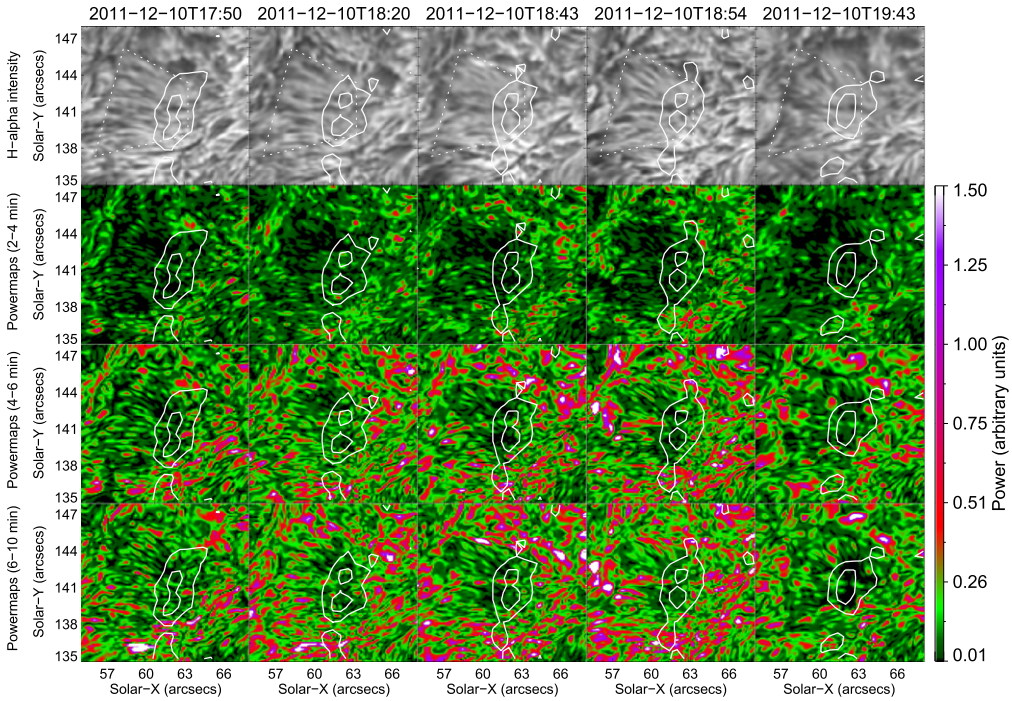

Figure 7. Time-resolved power maps and the respective intensity images for the Hα channel. Descriptions of the individual panels are the same as those described in Figure 4. Intensity images highlight horizontal canopy structures connected with the magnetic region. Power suppression properties are similar to those observed in the Ca II K channel. The polygon marked over the intensity images roughly encloses the power suppression region used in subsequent analysis.

locations demonstrating field strengths $\geqslant$500 G and $\geqslant$950 G as annotated. It is clear from these maps that the region between 4″ and 7″ distance (from the bottom of the slit) has relatively lower power across all period bands, which coincides with the locations of stronger magnetic fields. The time–distance maps in intensity reveal a brightening (albeit a darkening in Hα) at the center of the magnetic patch (at $\approx$6″) where the field strength is slightly weaker at certain times as indicated by the 950 G contour "islands." The intensity map in Ca II K (Figure 10) shows a clear oscillatory pattern with a periodicity of $\approx$4 minutes. A similar periodicity is also found in the HMI magnetic field measurements, suggesting they are likely to be magnetoacoustic waves. It is possible that they are driven by *p*-modes originating below the photosphere (see Jain et al. 2014;

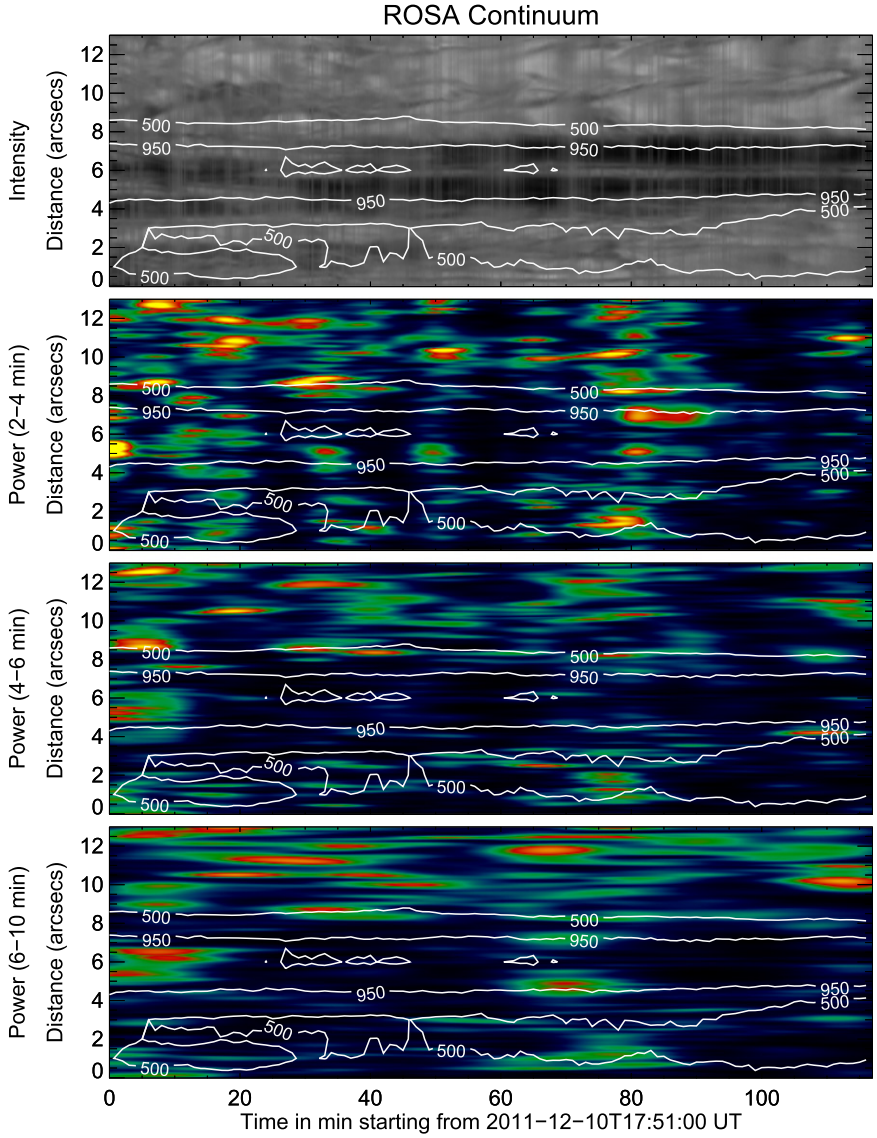

Figure 8. (From top to bottom) Time–distance maps of the continuum intensity and the corresponding power in the three period bands corresponding to 2–4, 4–6, and 6–10 minutes. These maps are constructed from the vertical green slit shown in Figure 2. Distance "0" corresponds to the bottom of the slit. The overplotted contours highlight the locations of magnetic fields at 500 and 950 G, as labeled. Stronger fields clearly coincide with locations of power suppression.

Krishna Prasad et al. 2015). In predominantly photospheric channels, the amplitudes are usually small, making them difficult to detect in the continuum and G-band channels and perhaps also the reason why they are not easily discernible in the more chromospheric Hα bandpass.

3.3. Temporal Variation of Power

While the time–distance power maps discussed in the previous subsection reveal the general spatial and temporal behavior of power in the suppression region, it is not clear whether there is any increase or decrease in power as the magnetic field evolves with time. Hence, we present here how the average power in the suppression region varies with time. To do this, first we interpolate HMI data both spatially and temporally to match the resolution of the ROSA channels. Then we identify the locations of strong magnetic fields (i.e., $\geqslant$950 G) at each instant and average the power contained within these locations for each period band to generate time evolving power. While scaling the HMI observations to the spatial and temporal resolutions of ROSA involves considerable interpolation, the revised HMI data is solely used to identify magnetic locations over which the ROSA/HARDcam power is averaged. Furthermore, we also verified our results by compressing the ROSA/HARDcam channels spatially and temporally to match the HMI resolution, which resulted in consistent outputs. Also, the power suppression regions in the Ca II K and Hα channels do not exactly coincide with the magnetic region as defined by HMI. Therefore, for these channels we selected a separate region bounded by the polygons marked in Figures 6 and 7, which roughly encloses the magnetic patch and the horizontal structures connected to it, and obtained the average power within that isolated region. The results are shown in Figure 12, where different colors represent the different period bands as annotated. The black curve represents the corresponding variation in the photospheric (HMI) magnetic field strength from the original, uninterpolated data. It appears that in general the power across all period bands decreases with increases in the magnetic field (i.e., it is

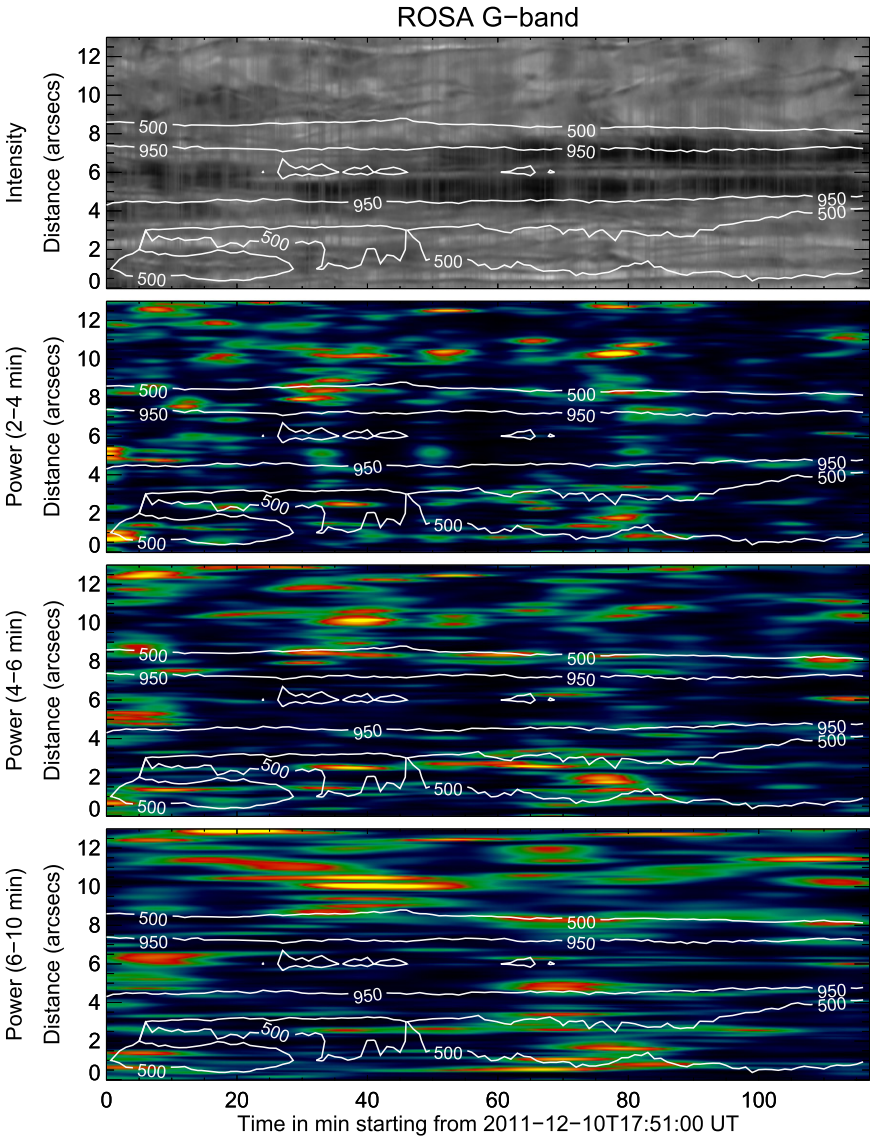

Figure 9. Same as Figure 8, but for the G-band channel. The strong field regions suppress the oscillatory power in all bands. The bright line at approximately 6″ in the intensity image coincides with the locations of occasional dips in magnetic field (as identified from the magnetic field contour "islands") and shows slight power enhancement in the 6–10 minute band.

anti-correlated). However, the power also appears to fluctuate with time, and naturally one would wish to check whether these small-scale fluctuations are also anti-correlated with changes in magnetic field. But this is difficult to accomplish because the power, which is proportional to the oscillation amplitude, also fluctuates in time due to closely spaced oscillation frequencies (Krishna Prasad et al. 2015). A closer inspection of the 4 minute oscillations seen in Ca II K indeed shows periodic variations in the amplitude, which resembles a beat pattern. To study the exact quantitative dependence of oscillation power on the magnetic field, we construct co-spatial and co-temporal power maps with HMI magnetic field, which are discussed in the following subsection.

3.4. Quantitative Dependence of Oscillation Power on Magnetic Field

So far we have shown that the oscillation power is suppressed in the presence of a magnetic field, and that the suppression becomes increasingly enhanced as the magnetic field strength increases. In this section, we study the exact quantitative dependence of oscillation power across different period bands on the magnetic field. To perform this, we compressed all the time-resolved power maps, both spatially and temporally, to construct co-spatial and co-temporal power maps with HMI magnetic field. This allowed us to make a one-to-one mapping of the oscillation power with the magnetic field. We then considered bins of 100 G and computed the means and standard deviations of oscillatory power contained within each period band, for each bin. The obtained mean values are plotted as diamonds in Figure 13 for each channel, with the corresponding standard deviations used to create the error bars. For the continuum and G-band channels, only those locations with a minimum magnetic field strength of 100 G are chosen. For Ca II K and Hα, this limit is set at 500 G. The reason a higher limit is imposed for these channels is that a large portion of the structures in the subfield appear to be connected to the magnetic region (see Figure 7), as previously described, which makes it less meaningful to map one-to-one

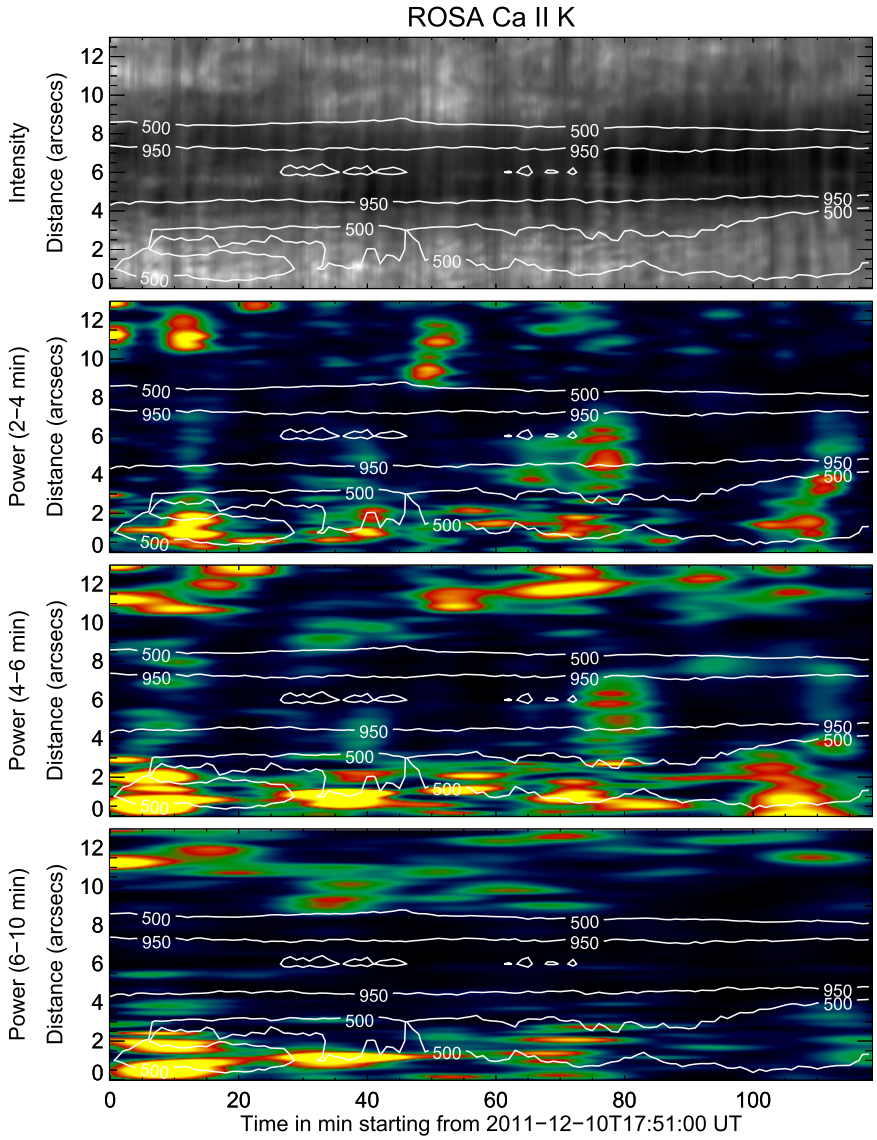

Figure 10. Same as Figure 8, but for the Ca II K channel. Power suppression again coincides with the locations of strong fields and appears to be more pronounced for longer periodicities. The intensity map clearly shows an oscillatory pattern with ≈4 minutes periodicity.

across the full subfield. Clearly, all the plots in Figure 13 show an enhanced suppression of power with increasing magnetic field strength. Here, we would like to emphasize that the error bars do not represent actual errors, but are instead the standard deviations for each value within the corresponding bin. Consequently, the extent of the error bars is smaller at higher field strengths as a result of more limited statistics.

In order to quantitatively compare suppression across different channels and period bands, the mean power values were fit linearly as shown in Figure 13. For the continuum and G-band data, separate fits were made for the full range of values (green line) and for values corresponding to magnetic field strengths above 500 G (red line). The last point in the Ca II K plot for the 2–4 minutes band (marked in red) was ignored as an outlier while making the fit. This is justified considering the poor statistics associated with the highest field strengths. The obtained gradients are listed in each plot in the figure. Comparing the gradient values across different period bands, it appears that the suppression is steeper for longer periods. A similar comparison across different channels (e.g., the continuum, G-band, and Hα), suggests that the suppression is also steeper at higher formation heights. The different behavior observed in the Ca II K plots is likely a result of its wide passband (≈1 Å) that naturally covers an extended range of solar atmospheric heights. In fact, Reardon et al. (2009) has shown that the contributions from bright photospheric wings swamp the dark chromospheric structures in Ca II K filtergrams, even for a bandpass narrower than that used in the present study.

3.5. Dominant Period

In this section we discuss the effects of evolving magnetic fields on the dominant periods and the corresponding spatial distributions. We identify peaks in the wavelet power spectra at each pixel and consider the period at the strongest peak (with highest power) as the dominant period. Because the wavelet analysis gives us time-resolved power spectra, we were able to construct *time evolving* dominant period maps. Power spectra

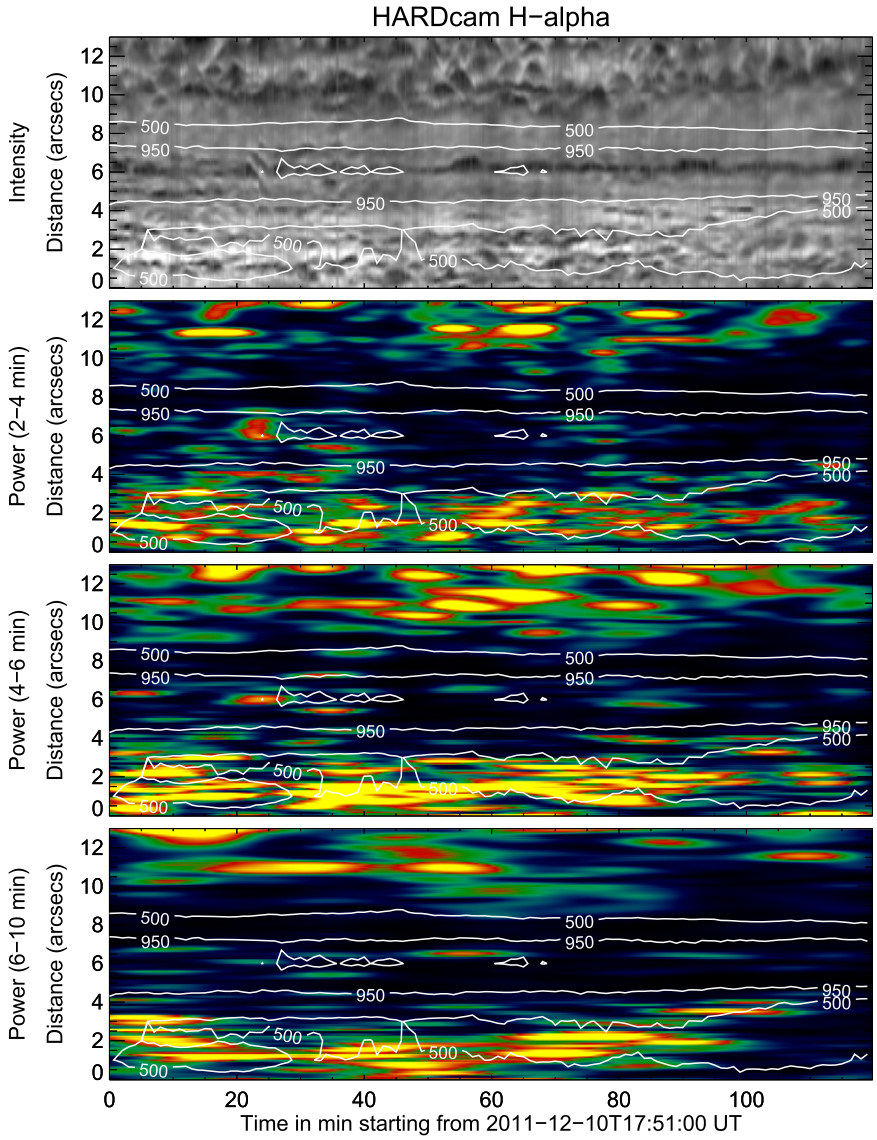

Figure 11. Same as Figure 8, but for the Hα channel. Power suppression properties are similar to those observed in the Ca II K channel. The bright line at 6″ is now replaced with a dark line in intensity, and is accompanied by occasional enhancements in power.

with periodicities only up to 10 minutes are considered in this analysis. The generated dominant period maps at five different instants during the observation period are shown in Figure 14 for all four channels. The white contours overplotted correspond to a magnetic field strength of 500 and 950 G. The continuum and G-band maps are dominated by red and yellow patches synonymous with longer (>6 minutes) periods. Although sparsely populated, the green and blue patches in these maps, corresponding to 5 minute and lower periods, are predominantly in the intergranular lanes (see Figures 4 and 5). However, the major magnetic concentration in this region does not seem to have any influence on the distribution of dominant periods seen in these maps. On the other hand, the Ca II K and Hα maps show preferentially shorter periods at the magnetic patch, alongside longer periods in the horizontal structures connected to it. The increasing green and blue colors found in the vicinity of the magnetic patch from the start of the time sequence to the end indicate the dominance of shorter periods with increasing field strength. The changing spatial distribution of the surrounding red/yellow patches in Ca II K is also worth noting.

Figure 15 shows a scatter plot of the dominant periods versus the magnetic field strengths for all four channels. All of the ROSA/HARDcam data have been compressed to match the HMI resolution, and are therefore similar to that described in Section 3.4. Again, only pixel locations corresponding to magnetic fields >100 G were considered for the continuum and G-band channels, and those corresponding to >500 G were included for the Ca II K and Hα channels. The overplotted solid lines in color show histograms of the dominant periods for the magnetic field ranges listed in the figure legend. Each histogram was normalized to its respective maximum before plotting. While the scatter plots indicate all of the possible dominant periods throughout the magnetic field range, the histograms suggest that many of the pixel locations have a dominant period >5 minutes in the continuum and G-band channels, irrespective of the strength of the field. A similar inference can also be drawn from the dominant period maps. However, it is important to note that the scatterplots

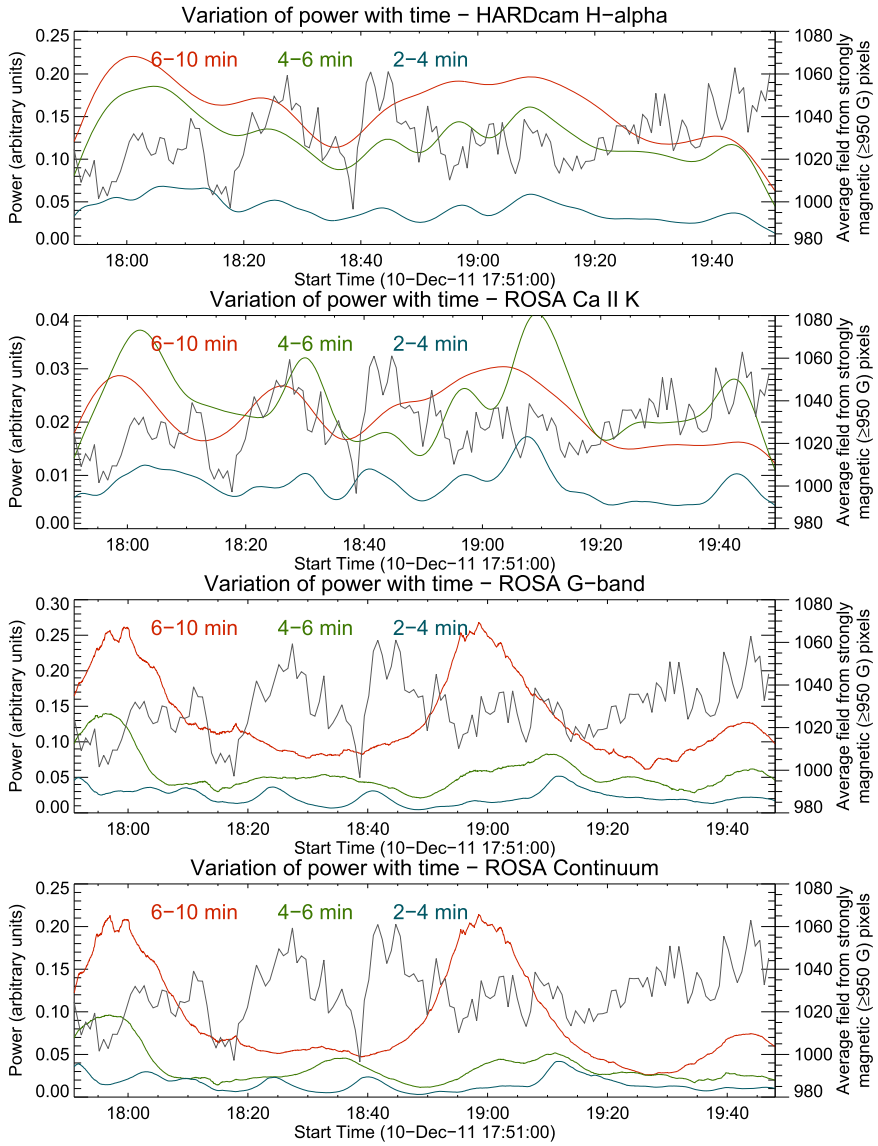

Figure 12. Variations in the average power for different period bands as a function of time. The four panels display results for the four channels studied. In each panel, red, green, and blue lines denote the time evolution of power for the different period bands as annotated. The black line represents the corresponding magnetic field evolution, with its axis shown on right. For the continuum and G-band channels, the power is averaged only from the strong magnetic field locations (≥950 G), whereas for the Ca II K and Hα channels, the power is averaged over the polygon marked in Figures 6 and 7.

include data from all temporal locations. Plots for Ca II K and Hα show that a majority of the pixel locations with stronger fields (>950 G) have a dominant period at ≈4 minute. This value is shifted to about 5 minutes for pixel locations with relatively weaker fields (500–950 G) in Ca II K. For Hα, the dominant period appears to have shifted to about 10 minutes for weaker field locations, but a significant fraction of them still show dominant power at ≈4 minutes. The difference in behavior of Ca II K and Hα channels in the weak field regime (i.e., at the locations between the outer and the inner contours shown in Figure 14) can also be understood to have arisen from their distinct passbands. The 1 Å wide Ca II K channel can have contributions from slightly inclined fields in the lower atmosphere, shifting the dominant period from 4 to 5 minutes, while the narrowband Hα channel has contributions mainly from the nearly horizontal structures (see Figure 7), which perhaps can raise the dominant period to ≈10 minutes.

4. CONCLUSIONS

Observations of active region NOAA 11372 reveal a reduction in *p*-mode oscillatory power (suppression) adjacent to a magnetic pore. The corresponding HMI LOS magnetic fields disclose a small magnetic concentration within this region, which is found to evolve with time. During the observation period, the magnetic element appears to change from a thin linear shape into a more uniform circular shape. The overall magnetic field strength for this element is also found to increase with time. We studied the effect of the evolving field on the time-dependent oscillatory power through the application of wavelet analysis. The power suppression regions in the continuum and G-band images are found to coincide with the locations of the magnetic element, whereas the power suppression found in the Ca II K and Hα images is spatially extended and asymmetrically distributed toward the left of the magnetic element. The asymmetric distribution of horizontal canopy structures in the chromosphere, which are

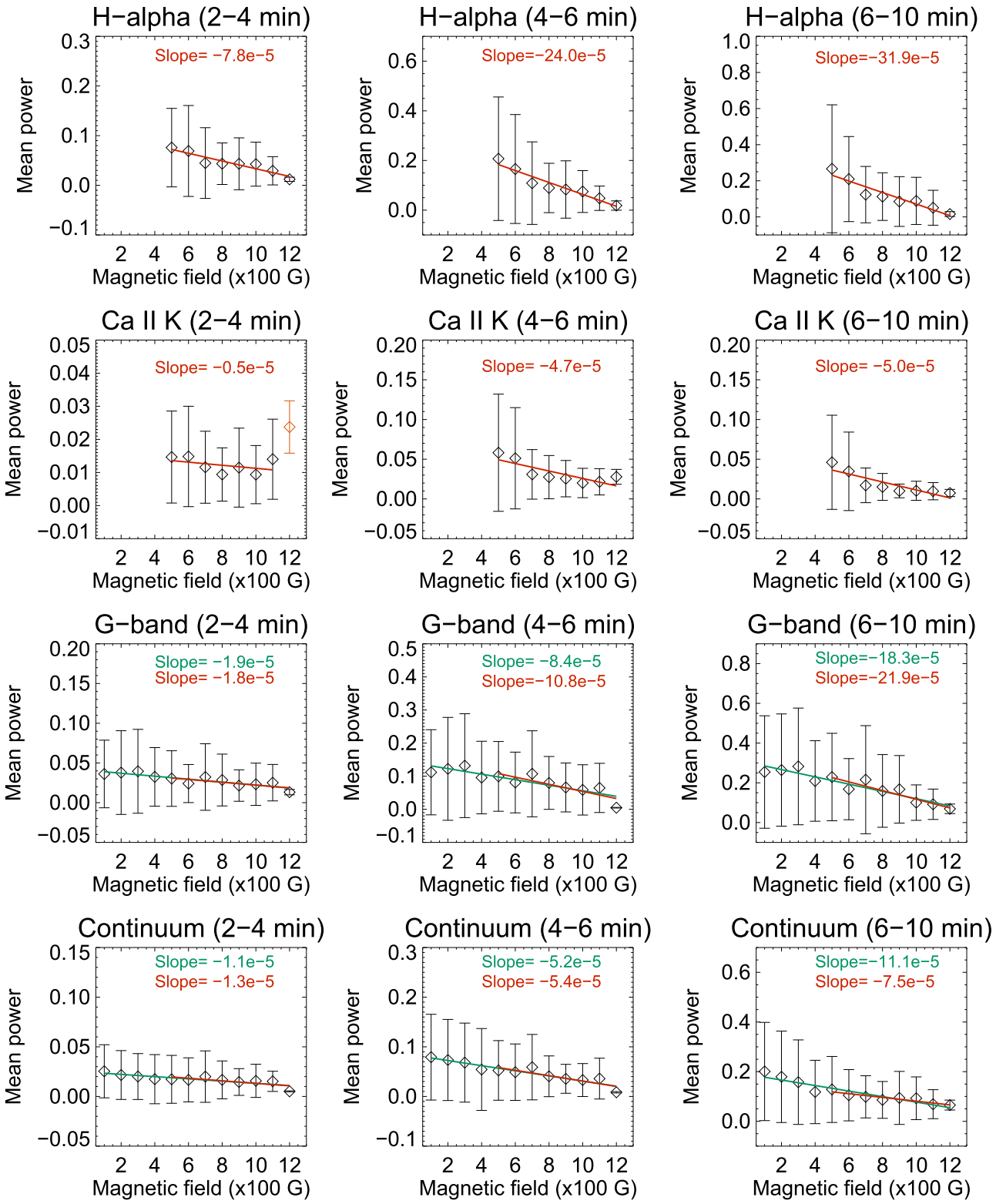

Figure 13. Dependence of the oscillatory power on the magnetic field strength across different channels and period bands as annotated. In each plot, diamonds represent the average power within a 100 G bin starting from that value, and the error bars denote the respective standard deviations. The overplotted sold lines are linear fits to the data. Locations with field strengths above 100 G are considered for the continuum and G-band channels, while fields above 500 G are considered for the Ca II K and Hα channels. Consequently, two different fits are performed for the photospheric channels (i.e., continuum and G-band; see the text for details). The last point in the Ca II K plot for the 2–4 minute band (shown in red) is discarded while making the fit. The obtained gradient values are listed in each plot. Oscillation power clearly decreases with increasing magnetic field strength.

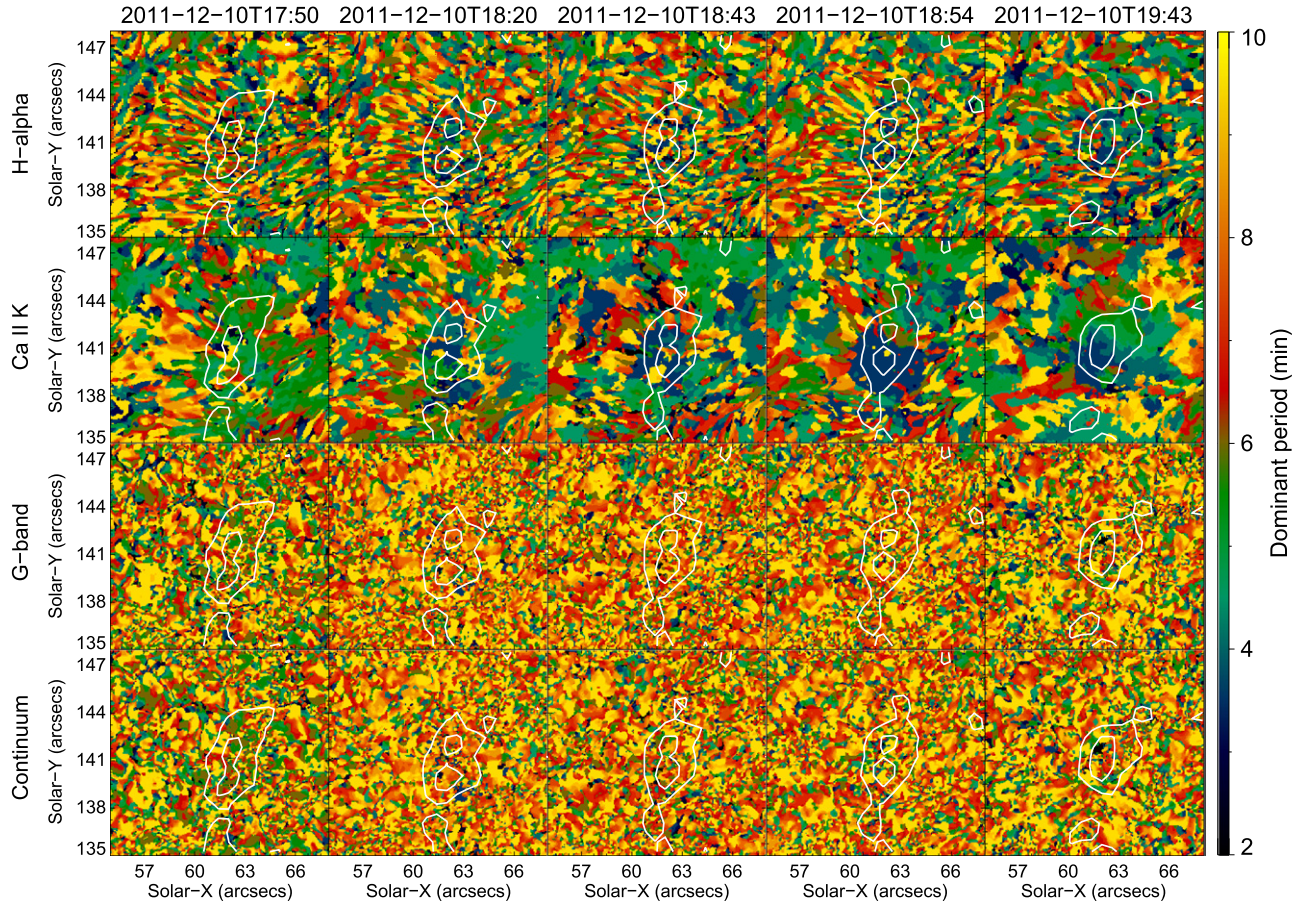

Figure 14. Dominant period maps (maps showing the period with the highest oscillatory power at each spatial location) in all four imaging channels at five different instants during the observations as annotated. Power spectra only in the 0–10 minute range are considered to generate these plots. The color scale is shown on the right, with the corresponding magnetic field contours overplotted similar to those displayed in Figures 4–7. Ca II K and Hα maps clearly show a drift toward shorter periods as the field strength increases with time.

connected to the magnetic region, most likely explains the different behavior in the latter channels. Power suppression is found to increase with time as the magnetic field is increased. Detailed analysis on the dependence of the oscillatory power on the magnetic field strengths revealed negative gradients, suggesting this is indeed true. A quantitative comparison of this dependence between different period bands and across different channels indicates that the power suppression is steeper for longer periods and at higher atmospheric heights.

Using a theoretical model, Jain et al. (2014) showed that the power deficit in the suppression region increases with height above the photosphere. They also found that this behavior manifests with a larger effect when the magnetic field is stronger, which explains the steeper dependence on magnetic field we found at larger heights. At the locations of higher field strengths, which were closer to the center of the magnetic element (see Figure 3), the magnetic fields are likely to be less inclined than those in the surroundings with relatively lower field strengths. This difference in inclination can cause more effective suppression in longer periods at higher field strengths (for instance, a recent study by Jess et al. 2013 demonstrates the effect of magnetic field inclination on the dominant oscillation period observed) and thus explains the steeper dependence of the oscillation power on the magnetic field for longer periods. We have not computed power suppression ratios to study the frequency dependence shown by Jain et al. (2014) and Hindman & Brown (1998) because our field of view mainly encompasses the active region and does not provide an inherently quiet region to make them statistically meaningful.

In addition, we studied the spatial distribution of the dominant period and its evolution with time. The dominant period extracted from the continuum and G-band intensities did not show any influence from the magnetic concentrations, whereas the Ca II K and Hα time series displayed shorter periods in the vicinity of stronger magnetic fields. Here, the dominant periodicity was also found to shorten with time as the magnetic field strength increased. Again, this behavior may be related to a decrease in the inclination of the field as the field strength increases.

The observed increase in the spatial extent of the suppression region with height is in agreement with the results of Moretti et al. (2007) and Jain et al. (2014). Moretti et al. (2007) explained their observations based on a mode-conversion model where the power suppression is primarily due to the partial conversion of p-modes into magnetoacoustic waves that go undetected (Cally et al. 2003). The model by Jain et al. (2014) also involves the generation of magnetoacoustic waves via the buffeting of p-modes, but here the power suppression is mainly a result of the difference in the evanescence of compressive waves within and outside the magnetic flux tube, producing shorter attenuation lengths inside the tube. In

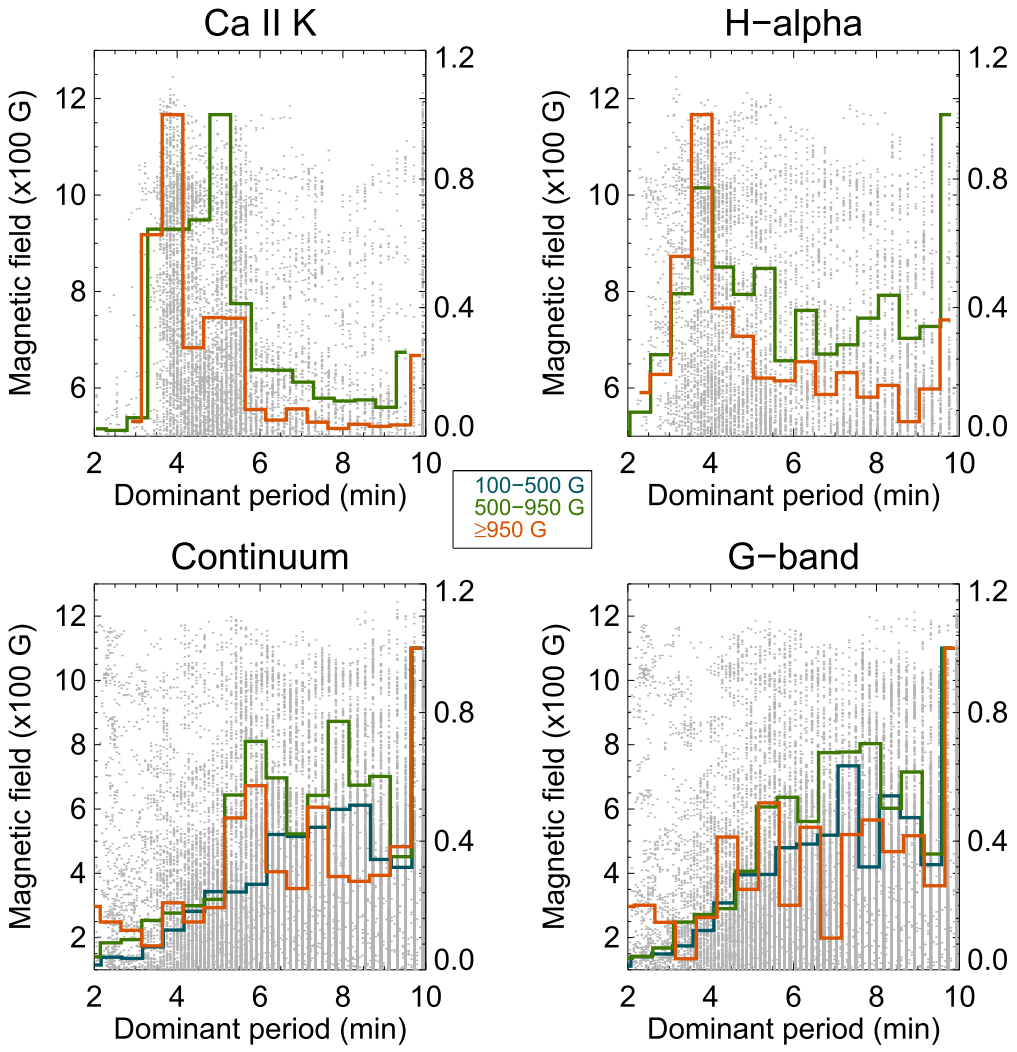

Figure 15. Scatter plots showing the dependence of the dominant period on the magnetic field strength for all four imaging channels. Locations with field strengths above 100 G are considered for the continuum and G-band channels, and those above 500 G are considered for the Ca II K and Hα channels. The overplotted solid lines show histograms for this data within different magnetic field ranges (listed in the legend at the center) as identified by their color. All the histograms are normalized to their respective maxima before plotting. The axis for the histograms is displayed on the right.

addition, each magnetic element is considered as a collection of thin magnetic fibrils where no radial structuring is present. Despite the differences, both models could reproduce the increasing spatial extent of the suppression region with atmospheric height. Therefore, the exact physical explanation behind these phenomena remains open and requires further theoretical and observational studies. In the near future we hope to utilize coordinated multi-height observations with spectropolarimetric sensitivites combined with realistic atmospheric models to address important issues such as the location of the equipartition ($\beta = 1$) layer with respect to the observed spectral lines, identifying the slow/fast nature of the observed oscillations, etc., that might help resolve this problem.

The authors thank the referee for useful comments. DBJ thanks STFC for an Ernest Rutherford Fellowship in addition to a dedicated standard grant that allowed this project to be undertaken. The HMI data used here are courtesy of NASA/SDO and HMI science teams.

Facilities: Dunn (ROSA, HARDcam), *SDO* (HMI).

REFERENCES

Beebe, H. A., & Johnson, H. R. 1969, SoPh, 10, 79
Bogdan, T. J., & Judge, P. G. 2006, RSPTA, 364, 313
Braun, D. C., Duvall, T. L., Jr., & Labonte, B. J. 1987, ApJL, 319, L27
Braun, D. C., Lindsey, C., Fan, Y., & Jefferies, S. M. 1992, ApJ, 392, 739
Brown, T. M., Bogdan, T. J., Lites, B. W., & Thomas, J. H. 1992, ApJL, 394, L65
Cally, P. S. 1995, ApJ, 451, 372
Cally, P. S., Crouch, A. D., & Braun, D. C. 2003, MNRAS, 346, 381
Chandrasekhar, S. 1952, PASP, 64, 98
Chitta, L. P., Jain, R., Kariyappa, R., & Jefferies, S. M. 2012, ApJ, 744, 98
Crouch, A. D., & Cally, P. S. 2003, SoPh, 214, 201
Goldreich, P., & Keeley, D. A. 1977, ApJ, 212, 243
Goldreich, P., & Kumar, P. 1988, ApJ, 326, 462
Gupta, G. R., Subramanian, S., Banerjee, D., Madjarska, M. S., & Doyle, J. G. 2013, SoPh, 282, 67
Hartlep, T., Kosovichev, A. G., Zhao, J., & Mansour, N. N. 2011, SoPh, 268, 321
Hindman, B. W., & Brown, T. M. 1998, ApJ, 504, 1029
Hindman, B. W., Jain, R., & Zweibel, E. G. 1997, ApJ, 476, 392
Jain, R., Gascoyne, A., Hindman, B. W., & Greer, B. 2014, ApJ, 796, 72
Jain, R., & Haber, D. 2002, A&A, 387, 1092
Jain, R., Hindman, B. W., & Zweibel, E. G. 1996, ApJ, 464, 476

Jess, D. B., De Moortel, I., Mathioudakis, M., et al. 2012a, ApJ, 757, 160
Jess, D. B., Mathioudakis, M., Christian, D. J., et al. 2010, SoPh, 261, 363
Jess, D. B., Reznikova, V. E., Van Doorsselaere, T., Keys, P. H., & Mackay, D. H. 2013, ApJ, 779, 168
Jess, D. B., Shelyag, S., Mathioudakis, M., et al. 2012b, ApJ, 746, 183
Judge, P. G., Tarbell, T. D., & Wilhelm, K. 2001, ApJ, 554, 424
Keys, P. H., Mathioudakis, M., Jess, D. B., Mackay, D. H., & Keenan, F. P. 2014, A&A, 566, A99
Kontogiannis, I., Tsiropoula, G., & Tziotziou, K. 2010, A&A, 510, A41
Kontogiannis, I., Tsiropoula, G., & Tziotziou, K. 2014, A&A, 567, A62
Krijger, J. M., Rutten, R. J., Lites, B. W., et al. 2001, A&A, 379, 1052
Krishna Prasad, S., Jess, D. B., & Khomenko, E. 2015, ApJL, 812, L15
Leighton, R. B., Noyes, R. W., & Simon, G. W. 1962, ApJ, 135, 474
Lites, B. W., White, O. R., & Packman, D. 1982, ApJ, 253, 386
Moretti, P. F., Jefferies, S. M., Armstrong, J. D., & McIntosh, S. W. 2007, A&A, 471, 961
Muglach, K. 2003, A&A, 401, 685
Pesnell, W. D., Thompson, B. J., & Chamberlin, P. C. 2012, SoPh, 275, 3
Rajaguru, S. P., Couvidat, S., Sun, X., Hayashi, K., & Schunker, H. 2013, SoPh, 287, 107
Reardon, K. P., Uitenbroek, H., & Cauzzi, G. 2009, A&A, 500, 1239
Rempel, M., Schüssler, M., & Knölker, M. 2009, ApJ, 691, 640
Rijs, C., Rajaguru, S. P., Przybylski, D., et al. 2016, ApJ, 817, 45
Rutten, R. J. 2007, in ASP Conf. Ser. 368, The Physics of Chromospheric Plasmas, ed. P. Heinzel, I. Dorotovič, & R. J. Rutten (San Francisco, CA: ASP)
Schou, J., Scherrer, P. H., Bush, R. I., et al. 2012, SoPh, 275, 229
Schüssler, M., & Vögler, A. 2006, ApJL, 641, L73
Tarbell, T. D., Peri, M., Frank, Z., Shine, R., & Title, A. M. 1988, in ESA Special Publication 286, Seismology of the Sun and Sun-Like Stars, ed. E. J. Rolfe (Noordwijk: ESA), 315
Title, A. M., Topka, K. P., Tarbell, T. D., et al. 1992, ApJ, 393, 782
Torrence, C., & Compo, G. P. 1998, BAMS, 79, 61
Vecchio, A., Cauzzi, G., Reardon, K. P., Janssen, K., & Rimmele, T. 2007, A&A, 461, L1
Vernazza, J. E., Avrett, E. H., & Loeser, R. 1981, ApJS, 45, 635
Woods, D. T., & Cram, L. E. 1981, SoPh, 69, 233